Earth and Planetary Science Letters 280 (2009) 194–204

Contents lists available at ScienceDirect

Earth and Planetary Science Letters

journal homepage: www.elsevier.com/locate/epsl

Cosmogenic ^{3}He and ^{21}Ne production rates calibrated against ^{10}Be in minerals from the Coso volcanic field

William H. Amidon [a,*], Dylan H. Rood [b], Kenneth A. Farley [a]

[a] California Institute of Technology, GPS Division, MS 100-23, Pasadena, CA 91125, United States
[b] Lawrence Livermore National Laboratory, P.O. Box 808, L-397, Livermore, CA 94550, United States

ARTICLE INFO

Article history:
Received 11 November 2008
Received in revised form 16 January 2009
Accepted 21 January 2009
Available online 25 February 2009

Editor: R.W. Carlson

Keywords:
helium
neon
^{10}Be
lithium
Li

ABSTRACT

This study calibrates the production rate of cosmogenic ^{3}He in pyroxene, olivine, garnet, zircon and apatite as well as ^{21}Ne in quartz and pyroxene against the known production rate of ^{10}Be in quartz. The Devil's Kitchen rhyolite from the Coso volcanic field in southeastern California (elev. ~1300 m) was chosen for this study due to its young age (~610 ka) and diverse mineral assemblage. Based on ^{10}Be, our two rhyolite samples have apparent exposure ages of ~49 and 93 ka, indicating substantial erosion after eruption. Combining data from the two samples, we estimate sea level high latitude ^{3}He spallation production rates of 145 ± 11, 141 ± 16, and 144 ± 30 at g^{-1} a^{-1} (2σ) for pyroxene, olivine and spessartine garnet respectively. For zircon and apatite, we estimate apparent ^{3}He spallation production rates of 114 ± 8 and 149 ± 28 at g^{-1} a^{-1} (2σ) respectively. The rates for zircon and apatite are reported as apparent production rates because we do not explicitly address the redistribution of spallation produced ^{3}He from adjacent minerals. These estimates quantitatively account for production of ^{3}He from both cosmogenic and radiogenic neutron reactions on ^{6}Li within the analyzed phases and also implanted from nuclear reactions in neighboring minerals; the high U, Th and Li content of this rhyolite provides a particularly rigorous test of this correction. We estimate ^{21}Ne production rates of 17.7 ± 1.6 and 34.1 ± 3.2 at g^{-1} a^{-1} (2σ) in quartz and pyroxene (Fe/Mg = 0.7 by mass) respectively. Although high U and Th contents create the potential for significant production of nucleogenic ^{21}Ne, this component is small due to the young eruption age of the rhyolite.

1. Introduction

Dating of geologic surfaces using cosmogenic ^{3}He or ^{21}Ne offers a fast and relatively simple alternative to cosmogenic dating using radioisotopes such as ^{10}Be and ^{26}Al (Gosse and Phillips, 2001). Although cosmogenic dating using ^{3}He has most often been performed on olivine and pyroxene, all major elements produce spallogenic ^{3}He as well as ^{3}H, which quickly decays to ^{3}He ($t_{1/2} = 12.5$ a). Therefore, cosmogenic ^{3}He dating can be applied to any mineral phase that is retentive to helium and for which the production rate of cosmogenic ^{3}He is known. The He retentivity of many mineral phases is well established (Dunai and Roselieb, 1996; Farley, 2002; Shuster and Farley, 2005; Copeland et al., 2007), but ^{3}He production rates remain uncertain.

Previous studies provide several ^{3}He production rate estimates for olivine and pyroxene (Kurz et al., 1990; Cerling and Craig, 1994; Licciardi et al., 1999; Dunai and Wijbrans, 2000; Ackert et al., 2003; Blard et al., 2006; Licciardi et al., 2006), a few estimates in garnet, zircon, apatite, titanite and kyanite (Gayer et al., 2004; Farley et al., 2006; Gayer et al., 2006; Amidon et al., 2008a), and some results on Fe–Ti oxides and calcite (Bryce and Farley, 2002; Kober et al., 2005; Amidon et al., 2008b). ^{3}He production rates in pyroxene and olivine range from ~100 to ~150 at g^{-1} a^{-1} at sea level and high latitude (SLHL), a wider range than for comparable calibration studies of ^{10}Be or ^{26}Al and outside of the stated analytical uncertainties. This large scatter may arise from incomplete or inaccurate consideration of one or more of the following factors: 1) significant amounts of ^{3}He can be produced by capture of radiogenic or cosmogenic slow neutrons by ^{6}Li (Andrews and Kay, 1982; Dunai et al., 2007), 2) newly created ^{3}He (and ^{3}H) nuclei experience redistribution into adjacent mineral phases due to their small size and high energy (Farley et al., 2006); 3) cosmogenic ^{3}He must be deconvolved from mantle-derived ^{3}He in common mafic phases (Kurz, 1986; Blard and Pik, 2008); 4) ^{3}He spallation production rates may not follow accepted elevation scaling laws (Gayer et al., 2004; Farley et al., 2006; Gayer et al., 2006; Amidon et al., 2008a).

Here we attempt to eliminate some of these sources of uncertainty and expand the utility of cosmogenic ^{3}He dating by cross-calibrating its production rate in pyroxene, olivine, garnet, zircon, and apatite against the known production rate of ^{10}Be in co-existing quartz. The rhyolite domes of the Coso volcanic field were chosen for this study because they are well studied petrographically and geochemically, and the Devil's Kitchen dome contains abundant coarse-grained crystals of all of the above mineral phases in a single rock (Manley and Bacon,

* Corresponding author. Tel.: +1 626 395 2190.
E-mail address: wamidon@gps.caltech.edu (W.H. Amidon).

0012-821X/$ – see front matter © 2009 Elsevier B.V. All rights reserved.
doi:10.1016/j.epsl.2009.01.031

2000). In addition, the high U, Th and Li of this rock presents an opportunity to develop and validate an approach to quantifying Li-produced ^{3}He in these phases.

2. Geologic overview

The Coso volcanic field is located in the southern Owens Valley, east of the Sierra Nevada Mountains. The focus of this study, the Devil's Kitchen rhyolite dome, has an ^{40}Ar/^{39}Ar isochron age of 0.613 ± 0.003 Ma (Simon et al., 2008). It contains an unusual assemblage of 0.1–1 mm sized phenocrysts including quartz, sanidine, plagioclase, magnetite, ilmenite, pyroxene, hornblende, biotite, olivine, and trace amounts of zircon and apatite (Bacon et al., 1981; Manley and Bacon, 2000). The rock typically exhibits a fine-grained (<10 μm) quartz–feldspar matrix. Of particular importance to this study is that the rhyolite is unusually rich in U, Th and Li, with concentrations of 14, 42, and 156 ppm respectively (Bacon et al., 1981). Zircons contain up to 2.5 wt.% of U, and up to 1.5 wt.% of Th (Miller and Wooden, 2004). The Devil's Kitchen rhyolite also contains dm-sized inclusions of a porphyritic andesite (Bacon and Metz, 1984). The andesitic inclusions contain 0.5 to 4 mm phenocrysts of plagioclase, as well as smaller (<few mm) phenocrysts of quartz, clinopyroxene, olivine, and Fe–Ti oxides. In addition to andesitic inclusions, one of our rhyolite samples (co-5) also contains small plagioclase-garnet xenoliths.

3. Methods

3.1. Sampling

Two closely-spaced localities were sampled on a low ridge on dome 28, at ~1333 m elevation (Bacon et al., 1980). Locality co-5 (N 36.03014, W 117.79654) was a flat bedrock surface about 40 cm above the alluvial surface of the ridge. A sample of the rhyolite (denoted co-5) was collected from the surface, along with an andesitic inclusion (sample co-5x). The inclusion measured approximately 10 × 8 × 5 cm and was sampled from an average depth of 8 cm directly below co-5. Locality co-6 (N 36.0299, W 117.79658), about 25 m away from co-5, was a bedrock knob rising about 80 cm above the surface of the ridge on the west side and about 2 m above the steeply sloping edge of the ridge on the east side. Again a rhyolite sample (co-6) was collected from the surface and an andesitic inclusion (sample co-6x, from an average depth of 5 cm) directly below this surface. The inclusion measured approximately 12 × 7 × 7 cm in dimension.

We thus have four rock samples for analysis: one rhyolite and one andesitic inclusion from each of two localities. The two lithologies from each location will have the same cosmic ray exposure history after correction for the sub-surface depth at which the inclusion was located. Similarly, we assume that the chemical composition of each lithology is the same at the two localities (see Appendix A). As we show below, the two localities have very different exposure histories, providing us the opportunity to see how ^{3}He concentrations vary with the total cosmic ray exposure derived from ^{10}Be.

No topographic shielding corrections are necessary at either locality, nor do we attempt to correct for shielding by snow or ice. Ignoring these corrections is further justified by the fact that we are comparing ^{3}He and ^{21}Ne directly to ^{10}Be, so shielding effects should cancel when production rates are calculated.

Mineral separations were done following standard heavy liquid procedures followed by HF leaching of quartz for ^{10}Be and ^{21}Ne analysis. All samples were handpicked of contaminant phases prior to analysis.

3.2. ^{10}Be analyses and ^{10}Be production rate

Analysis of ^{10}Be concentrations in quartz was performed at Lawrence Livermore National Laboratory (LLNL). Quartz samples were purified by HF leaching following Kohl and Nishiizumi (1992), and Be was extracted and analyzed following standard LLNL procedures. Measured ^{10}Be/^{9}Be ratios are normalized to the 07KNSTD3110 with a ^{10}Be/^{9}Be ratio of 2.85×10^{-12}, based on a ^{10}Be half life of 1.36 million years (Niishizumi et al., 2007). To calculate ^{3}He and ^{21}Ne production rates we adopt a SLHL ^{10}Be production rate of 4.87 at g^{-1} a^{-1}. This is based on the average production rate published in Balco et al. (2008) scaled following Lifton et al. (2005), and reduced by a factor of 0.904 to reflect the newly adopted ^{10}Be half life mentioned above. This ignores muogenic production of ^{10}Be, which should be ~2–3% of spallogenic production (Heisinger et al., 2002a,b).

3.3. Helium analyses

Samples were analyzed for ^{3}He either directly as obtained from mineral separation or after crushing, either in vacuum or in air. Crushing is required in some mineral phases to release and/or measure magmatic helium contained in inclusions. Samples crushed under vacuum were crushed for 3 min in a steel tube following published procedures (Patterson et al., 1997). After crushing either on-line or in air sample material was wet-sieved through a 24 μm sieve and recrushed as necessary until all material was smaller than 24 μm. Three samples were re-crushed for a second 3 minute cycle and analyzed to verify that all ^{3}He is removed during the initial crushing phase. None of the zircon or apatite samples were crushed prior to analysis, under the assumption that the magmatic ^{3}He component is negligible in these very fine grained phases.

Only grains from the >150 μm size fraction were used during analysis of pyroxene, olivine and garnet, making the effect of implanted ^{3}He from adjacent mineral phases negligible. To document the effect of implanted ^{3}He on fine-grained phases, zircons were sieved into grain size fractions if enough sample material was available. The average dimensions of mineral grains are expressed in terms of the equivalent radius of a sphere with the same surface area to volume ratio (Farley et al., 1996).

Extraction of matrix-sited ^{3}He was performed by diffusing helium gas out of the sample either by heating to ~1300 °C in a double-walled resistance furnace, or to similar temperatures by heating with a Nd-YAG laser in a Pt capsule. Complete helium extraction from each sample was verified by re-extracts under identical heating conditions. In both cases, helium was purified by exposure to hot and cold SAES getters, and was cryogenically focused on charcoal at 12 K before release of He at 32 K into a MAP 215-50 mass spectrometer. Sensitivity of the mass spectrometer was determined by analysis of gas standards at similar helium pressures and ^{3}He/^{4}He ratios to the samples being analyzed. The precision of our measurements can be estimated from five replicate analyses of sample co-5x (pyroxene), which gave a 1σ standard deviation of ~5.5% for ^{3}He counting rates of 5–10 cps. Zircon and apatite were typically measured at lower counting rates of 1–3 cps, a range in which replicate standards yield a 1σ standard deviation of ~8% on ^{3}He.

3.4. ^{21}Ne analyses

Uncrushed quartz samples were either heated in a single step to 1300 °C or step-heated at 250, 800, and 1300 °C to preferentially release matrix-sited neon from adsorbed or inclusion-held neon (Niedermann, 2002). None of the 250 or 1300 °C steps contained excess ^{21}Ne, although the 1300° step contained large air components. Pyroxene was either heated in a single temperature step at ~1500 °C, or fused by rastering a Nd-YAG laser over bare grains. Neon was purified over hot and cold SAES getters and then cryogenically focused at 32 K on charcoal before release at 75 K into a GV Helix-SFT split tube mass spectrometer operating in peak-jumping mode on the electron multiplier spur. Because the ^{40}Ar^{++} peak is resolved from the ^{20}Ne^{+} peak, no correction for the ^{40}Ar isobar was applied. Corrections for the $^{44}CO_2$ isobar were <2% and were made by determining a $^{44}CO_2^{++}/^{44}CO_2^{+}$

ratio of 0.0153 ± 0.0003 for CO_2 signals which were constant to ± 10% for all samples, standards and blanks. Mass fractionation corrections of 1.1% per AMU based on air standards were applied. The precision on Ne concentrations is estimated to be ~7% (1σ standard deviation) based on five replicate analyses of sample co-6 (quartz).

3.5. Li analysis

Lithium measurements were made on a Thermo-Finnagan Element 1 single-collector ICPMS, using isotope dilution with a ^{6}Li spike calibrated with a commercial Li normal solution. Measurements were made on ~1 mg of handpicked material, but not the same aliquots used for ^{3}He analysis. Most samples were dissolved on a hot plate in a 2:1 HF:HNO_3 cocktail except for zircons, which were Parr bombed in HF, redissolved in HCl, and finally in HNO_3. Reproducibility of Li measurements was established by performing at least two replicate measurements on separately picked aliquots of each sample. If agreement within 15% was not achieved, additional aliquots were analyzed. Lithium blanks typically total less than 0.1% of measured lithium, with a maximum of ~2%. The sample cleaning procedure, and a 2σ external precision of ~12% are established and discussed by Amidon et al. (2008a).

3.6. Determining average host mineral Li contents

The capture of low energy neutrons on ^{6}Li produces ^{3}He via the reaction ^{6}Li(n,α)^{3}H(β$^-$)^{3}He (Andrews and Kay, 1982). These tritium nuclei have an average energy of ~2.7 MeV and a stopping range of ~30 μm in apatite and zircon (Ziegler, 2003; Farley et al., 2006). Although apatite and zircon are low in Li, their small grain size makes them vulnerable to implantation of Li-produced ^{3}He from adjacent Li-rich phases, e.g., biotite. As a result, calculation of the total Li-derived ^{3}He in apatite and zircon requires knowledge of the average Li content of the immediately adjacent minerals. To establish this quantity, individual zircon and apatite crystals were identified in polished sections of rock and their minimum and maximum dimensions as well as the relative proportion of their surface area in contact with each adjacent mineral were documented. One dataset was generated for the andesitic inclusions (co-5x/6x) and another for the host rhyolite samples (co-5/6) for grains of minimum dimension of 20 μm. Multiplying the fractional contact area of each adjacent mineral phase by its measured Li content and summing over all mineral phases gives the average Li content surrounding the mineral of interest (Online Table A4).

4. Results

4.1. ^{10}Be results

The quartz in sample co-5 has a ^{10}Be concentration of 0.637 ± 0.015 Mat/g, compared to 1.202 ± 0.019 Mat/g for sample co-6 (Table 1). These quite different concentrations are factors of ~11.6 and ~6.1 lower than expected for a 0.613 Ma uneroded/unburied surface and give a $^{10}Be_{co5}/^{10}Be_{co6}$ ratio of 0.53. As discussed below, the simplest interpretations of these ^{10}Be concentrations are either as apparent exposure ages of ~49 and 93 ka, or as steady-state erosion rates of ~0.070 and 0.036 mm/yr respectively (Bierman, 1994).

Table 1
Results of ^{10}Be analysis in quartz.

Sample	$(^{10}Be/^{9}Be)_{blank}$	$^{10}Be_{blank}$ (atoms)	$(^{10}Be/^{9}Be)_{samp}$	$^{10}Be_{samp}$ (Mat/g)	1σ SD (Mat/g)
CO-5	1.41E−15	18473	2.97E−13	0.637	0.015
CO-6	1.41E−15	18538	8.22E−13	1.201	0.019
C3_C4	1.40E−15	23085	9.77E−13	2.918	0.078

Results reported relative to the 07KNSTD3110 standard. C3_C4 from Farley et al. (2006).

Table 2
Crushing analyses.

Sample	Mass (mg)	^{3}He (Mat/g)	1σ SD (Mat/g)	^{4}He (ncc STP/g)	1σ SD (ncc STP/g)	^{3}He/^{4}He (Ra)	1σ SD (Ra)
Pyroxene							
co5-p-1	6.21	1.4	0.1	80.3	2.2	0.5	0.05
co5x-p-1	85.70	6.3	0.4	19.5	0.8	8.7	0.6
co5x-p-2	21.20	6.3	0.5	20.5	0.9	8.3	0.7
co5x-p-3	43.40	6.6	0.5	20.7	0.8	8.5	0.7
Mean co5x		**6.4**		**20.2**		**8.5**	
co6-p-1	8.84	2.2	0.2	64.4	2.3	0.9	0.1
co6-p-2	13.70	3.2	0.3	18.9	0.7	4.5	0.4
Mean co6		**2.7**	**0.3**	**41.6**		**2.7**	
co6x-p-1	99.00	7.5	0.4	22.5	0.6	8.9	0.5
co6x-p-2	18.90	7.1	0.4	23.1	0.7	8.2	0.6
co6x-p-3	29.78	7.2	0.5	22.7	0.6	8.5	0.6
Mean co6x		**7.3**		**22.8**		**8.6**	
Olivine							
co5-o-1	7.90	0.01	0.00	11.9	0.5	0.01	0.01
co6-o-1	8.42	0.02	0.01	74.5	2.0	0.01	0.004
co5x-o-1	23.31	0.8	0.1	5.1	0.3	4.0	0.7
co6x-o-1	11.51	0.6	0.1	5.1	0.3	3.4	0.6
Garnet							
co5-g-1	10.63	0.8	0.1	1580.3	39.5	0.01	0.002
Hornblende							
co5-h-1	10.00	0.4	0.1	9.1	0.2	1.2	0.3
Re-crush data							
co5x-p1-RC	85.7	0.15	–	0.01	–	–	–
co6-p1-RC	8.8	0.02	–	0.02	–	–	–
co5x-o1-RC	23.3	0.00	–	0.00	–	–	–

4.2. Helium results

Results of helium extracted by crushing are presented in Table 2. Pyroxenes and olivines from the andesitic inclusions (samples co-5x/6x) give much higher concentrations of ^{3}He during crushing than those from the host rhyolite, with pyroxene giving about an order of magnitude more ^{3}He than olivine in both cases. The pyroxenes from co-5x/6x yield ^{3}He/^{4}He ratios near 8 Ra, suggesting they contain a significant mantle-derived component, whereas most other mineral phases give intermediate to radiogenic ^{3}He/^{4}He ratios (0.01–4 Ra). Results of degassing of matrix sited helium in pyroxene, olivine, and garnet are presented in Table 3 and Fig. 1. Samples co-5/5x and co-6/6x are found to have ~23 and ~41 Mat/g of ^{3}He respectively, for a $^3He_{co5/5x}/^3He_{co6/6x}$ ratio of about 0.56, quite similar to the ratio of 0.53 observed in the ^{10}Be data. Results of ^{3}He released by laser heating of uncrushed zircon and apatite are presented in Table 4 and Fig. 2. A strong correlation is observed between grain size (equivalent radii 33–78 μm) and total measured ^{3}He concentration in zircon. This grain size range is correlated with a range of ^{3}He concentrations between 23 and 37 Mat/g in co-5/5x and ~39 to 62 Mat/g in co-6/6x. Analyses of apatite aliquots with equivalent radii of ~100 μm from samples co-5x and co-6x yield 23.8 and 44.6 Mat/g respectively, giving a $^3He_{co5x}/^3He_{co6x}$ ratio of 0.53.

4.3. Neon results

Results of neon analyses are presented in Table 5 and Fig. 3. Measured ^{21}Ne/^{20}Ne and ^{22}Ne/^{20}Ne ratios in hand-picked quartz samples plot within error of the air–cosmogenic mixing line for quartz on a three-isotope diagram (Niedermann et al., 1993). In addition, two analyses were made of inclusion bearing quartz extracted from the samples; these plot well away from the air–cosmogenic mixing line.

Table 3
Helium analyses in pyroxene, olivine, garnet, hornblende, and quartz.

Sample		Mass (mg)	$^{3}He_{m}$ (Mat/g)	$^{3}He_{cc}$ (Mat/g)	1σSE (Mat/g)	$^{3}He_{cn+nuc+mu}$ (Mat/g)	1σSD (Mat/g)	$^{3}He_{sp}$ (Mat/g)	$^{3}He_{sp\ (z=0)}$ (Mat/g)	1σSE (Mat/g)	$^{4}He_{m}$ (ncc STP/g)	$^{4}He_{(cc)}$ (nccSTP/g)	$^{3}He/^{4}He$ (Ra)	Eq. Rad. (μm)	^{10}Be (Mat/g)	1σSD (Mat/g)	$^{3}He_{sp}/^{10}Be$	1σ SE	PR (at $g^{-1}a^{1}$)	1σ SE (at $g^{-1}a^{-1}$)
Pyroxene																				
co5-p-1	c	10.62	24.8	24.8		4.5	0.9	20.3	20.3		277	277	2.4	155						
co5-p-2	uc	2.53	22.7	21.3		4.5	0.9	16.8	16.8		617	536	1.0	161						
co5-p-3	uc	2.78	24.9	23.5		4.5	0.9	19.0	19.0		763	683	0.9	153						
Mean			**24.1**	**23.2**	**1.3**		**0.9**		**18.7**	**1.6**		**499**			**0.637**	**0.015**	**29.3**	**2.6**	**142.8**	**14.1**
co5x-p-1	c	39.47	22.4	22.4		3.9	0.8	18.5	20.8		165	165	3.6	225						
co5x-p-2	c	10.91	21.6	21.6		3.8	0.8	17.9	20.0		19	19	30.2	232						
co5x-p-3	c	37.56	21.1	21.1		3.8	0.8	17.3	19.4		35	35	16.0	230						
co5x-p-4	uc	10.08	28.2	21.7		3.7	0.8	18.0	20.2		66	47	11.4	239						
co5x-p-5	uc	10.03	25.9	19.4		3.7	0.8	15.7	17.6		70	50	10.0	234						
Mean			**23.9**	**21.3**	**0.6**		**0.8**		**19.6**	**1.0**		**63**			**0.637**	**0.015**	**30.8**	**1.7**	**149.9**	**10.8**
co6-p-1	c	7.00	41.8	41.8		4.5	0.9	37.3	37.3		99	99	11.3	186						
co6-p-2	c	6.93	39.7	39.7		5.4	1.1	34.3	34.3		587	587	1.8	119						
Mean			**40.7**	**40.7**	**1.5**		**1.0**		**35.8**	**1.8**		**343**			**1.201**	**0.019**	**29.8**	**1.6**	**145.1**	**10.2**
co6x-p-1	c	46.63	39.3	39.3		7.2	1.5	32.1	34.5		245	245	4.3	252						
co6x-p-2	c	9.95	40.6	40.6		7.7	1.6	32.9	35.4		80	80	13.6	232						
co6x-p-3	c	7.05	42.0	42.0		7.9	1.7	34.1	36.6		18	18	64.1	225						
co6x-p-4	uc	14.90	46.0	38.7		7.5	1.6	31.1	33.5		118	97	10.4	238						
co6x-p-5	uc	18.95	46.4	39.1		7.4	1.5	31.7	34.1		288	269	4.3	244						
Mean			**42.9**	**39.9**	**0.7**		**1.6**		**34.8**	**1.7**		**142**			**1.201**	**0.019**	**29.0**	**1.5**	**141.2**	**10.3**
														Weighted mean for pyroxene			***29.7***	***0.9***	***144.9***	***5.5***
Olivine																				
co5-o-1	c	5.80	22.0	22.0		3.3	0.7	18.7	18.7		630	630	0.9	124						
co5-o-2	uc	1.59	20.8	20.8		3.1	0.6	17.8	17.8		30725	30713	0.02	143						
Mean			**21.4**	**21.4**	**0.8**		**0.7**		**18.3**	**1.1**		**15671**			**0.637**	**0.015**	**28.6**	**1.8**	**139.5**	**11.4**
co5x-o-1	c	17.46	19.9	19.9	2.0	4.6	1.0	15.4	17.2	2.2	84	84	6.4	198	0.637	0.015	27.0	3.5	131.6	18.5
co6-o-1	c	6.00	43.1	43.1	4.3	5.2	1.1	38.0	38.0	4.4	222	222	4.3	156	1.201	0.019	31.6	3.7	154.0	19.9
co6x-o-1	c	5.99	41.2	41.2	4.1	8.2	1.7	33.0	35.4	4.5	73	73	15.2	227	1.201	0.019	29.5	3.8	143.7	19.7
														Weighted mean for olivine			***28.9***	***1.4***	***141.0***	***8.0***
Garnet																				
co5-g-1	c	6.56	26.5	26.5		7.2	1.5	19.3	19.3		23024	23024	0.03	144						
co5-g-2	uc	2.13	25.7	24.9		7.2	1.5	17.7	17.7		23999	22419	0.03	167						
co5-g-3	uc	3.39	27.7	26.9		7.2	1.5	19.7	19.7		25599	24019	0.03	168						
Mean			**26.6**	**26.1**	**0.7**		**1.5**		**18.9**	**1.7**		**23154**			**0.637**	**0.015**	**29.7**	**2.7**	**144.4**	**15.2**
Hornblende																				
co5-h-2	uc	2.24	39.6	39.2		26.1	5.5	13.1	13.1		3258	3249	0.3	143						
co5-h-3	uc	2.20	41.2	41.2		26.2	5.5	15.0	15.0		10658	10649	0.1	147						
Mean			**40.4**	**40.2**	**1.5**		**5.5**		**14.0**	**5.7**		**6949**			**0.637**	**0.015**	**22.0**	**8.9**	**107.3**	**43.8**
Quartz																				
co5-q-1	uc	33.75	2.3	2.3	0.2	-		-	2.3		9	9	6.6	169	-		-		-	
co5-q-2	uc	33.80	2.3	2.3	0.2	-		-	2.3		7	7	8.9	172	-		-		-	
Mean									**2.3**			**8**								
co6-q-1	uc	31.34	3.2	3.2	0.3	-		-	3.2		10	10	8.3	173	-		-		-	
co6-q-2	uc	29.54	2.2	2.2	0.2	-		-	2.2		3	3	20.6	175	-		-		-	
Mean									**2.7**			**7**								

c = crushed prior to heating; uc = uncrushed prior to heating; $^{3}He_{m}$ = measured during heating; $^{3}He_{cc}$ = after subtraction of crushing-released magmatic component (if necessary).
$^{3}He_{cn+nuc+mu}$ = calculated concentration of all Li-produced ^{3}He components; $^{3}He_{sp}$ = after subtraction of Li-produced components; $^{3}He_{sp\ (z=0)}$ after correction for sampling depth (if necessary).
$^{4}He_{m}$ = measured during heating; $^{4}He_{cc}$ = corrected for crushing-released magmatic component (if necessary); Eq. Rad. = mean equivalent spherical radius calculated following Farley et al. (1996).

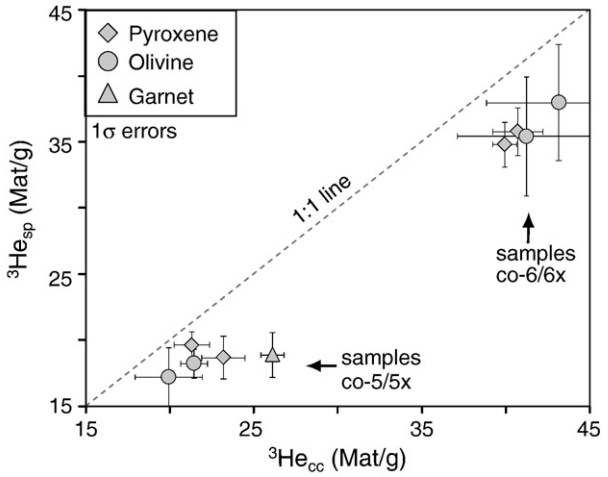

Fig. 1. Spallogenic ^3He ($^3He_{sp}$) vs. crush-corrected ^3He ($^3He_{cc}$) in pyroxene, olivine, and garnet. Samples plot to the left of the 1:1 line owing to the presence of Li-produced ^3He. Each of the four data points for pyroxene and olivine represents the mean for a given sample (i.e. co5, co6, co5x and co6x). Garnet was only found in sample co5.

Four samples of pyroxene degassed at 1500 °C also plot within error of the air–cosmogenic mixing line for quartz, and are statistically indistinguishable from the mixing line of lower slope proposed for pyroxene (Schafer et al., 1999). Two additional pyroxene samples degassed by complete fusion of the grains using a laser give $^{21}Ne/^{20}Ne$ and $^{22}Ne/^{20}Ne$ ratios that plot away from the mixing line, and closer to the MORB line (Staudacher and Allegre, 1993).

4.4. Li concentrations

Results of Li analyses are summarized in Table 6. Concentrations of Li are high in most minerals, ranging from a minimum of ~1.4 ppm in some zircons to >5000 ppm in biotite. Zircon and apatite cluster from 1–15 ppm, olivine and pyroxene from 25–50 ppm, quartz and garnet near 100 ppm, and feldspars around 150 ppm.

The distributions of minerals adjacent to apatite and zircon (Section 3.6) and their associated Li content are presented in supplementary Table A4. These differ significantly between the rhyolite (co-5/6) and the andesitic inclusions (co-5x/6x). Zircons in the rhyolite are primarily in contact with matrix material, which in combination with a small amount of high-Li biotite gives an average Li content of 430–668 ppm. In the andesitic inclusions, zircons and apatites are in contact primarily with feldspar and matrix material, with average Li contents of 360–400 ppm. In both cases, average Li contents of adjacent mineral assemblages are extremely high, and are most sensitive to small amounts of contact area with biotite, a high Li phase.

4.5. Compositional analysis

Mineral compositions were determined using the JEOL JXA-8200 electron microprobe at Caltech, and are summarized in supplementary Table A1. Pyroxenes have an augitic composition averaging $(Ca_{0.83}, Na_{0.02})(Mg_{0.76},Fe_{0.23},Al_{0.28})(Si_{1.8},Al_{0.28})O_6$. Olivines average Fo_{76}, with very little compositional variation. Garnets have a spessartine/almandine composition averaging $(Mn_{1.57},Ca_{0.17},Mg_{0.12},Fe_{1.33})Al_{1.8}Si_3O_{12}$.

5. Data interpretation

5.1. Interpretation of measured ^3He

Several lines of evidence suggest that the ^3He in all five minerals is dominantly cosmogenic. First, measured $^3He_{co5/5x}/^3He_{co6/6x}$ ratios for

Table 4
Helium analyses in zircon and apatite.

Sample	Mass (mg)	^3He_m (Mat/g)	1σSD (Mat/g)	$^3He_{cn+nuc+mu}$ (Mat/g)	1σSD (Mat/g)	$^3He_{sp}$ (Mat/g)	$^3He_{sp\ (z=0)}$ (Mat/g)	1σSE (Mat/g)	^4He_m (ncc STP/g)	$^3He_m/^4He_m$ (Ra)	Eq. Rad. (μm)	^{10}Be (Mat/g)	1σSD (Mat/g)	$\frac{^3He_{sp}}{^{10}Be}$	1σSE	PR (at $g^{-1}a^{-1}$)	1σSE (at $g^{-1}a^{-1}$)
Zircon																	
co5-z-1	6.32	23.2	1.9	9.0	2.2	14.2	14.2		274	0.002	78						
co5-z-2	1.39	24.3	1.9	9.4	2.3	14.9	14.9		222	0.003	74						
co5-z-3	1.24	30.2	2.4	13.8	3.5	16.4	16.4		302	0.003	49						
co5-z-4	1.29	30.2	2.4	13.8	3.5	16.4	16.4		292	0.003	48						
co5-z-5	1.33	36.8	2.9	19.1	4.8	17.7	17.7		423	0.002	33						
Mean		**28.9**					**15.9**	**0.7**				**0.637**	**0.015**	**25.0**	**1.2**	**121.5**	**8.2**
co6-z-1	4.33	54.0	4.3	25.8	6.5	28.2	28.2		302	0.005	58						
co6-z-2	3.32	62.5	5.0	35.5	8.9	27.0	27.0		357	0.005	41						
Mean		**58.3**					**27.6**	**0.8**				**1.201**	**0.019**	**23.0**	**0.8**	**112.0**	**6.5**
co5x-z-1	4.78	24.6	2.0	11.3	2.8	13.3	15.0	3.4	76	0.009	48	0.637	0.015	23.5	5.4	114.3	27.6
co6x-z-1	4.04	39.3	3.1	13.8	3.5	25.5	27.4		38	0.027	68						
co6x-z-2	5.73	43.9	3.5	17.5	4.4	26.4	28.4		71	0.017	53						
co6x-z-3	5.06	47.8	3.8	22.2	5.6	25.6	27.5		75	0.017	41						
Mean		**43.7**					**27.8**	**0.4**				**1.201**	**0.019**	**23.1**	**0.5**	**112.6**	**5.7**
												Weighted mean for zircon		***23.3***	***0.4***	***114.3***	***3.8***
Apatite																	
co5x-a-1	4.56	23.8	1.9	6.4	1.6	17.4	19.5	2.5	1.8	0.346	100	0.637	0.015	30.6	4.0	149.0	20.9
co6x-a-1	3.06	44.6	3.6	10.5	2.6	34.1	36.6	4.4	11.5	0.104	101	1.201	0.019	30.5	3.7	148.6	19.8
												Weighted mean for apatite		***30.6***	***2.7***	***148.8***	***14.4***

All samples uncrushed; ^3He_m = measured during heating; $^3He_{cn+nuc+mu}$ = calculated concentration of all Li-produced ^3He components; $^3He_{sp}$ = after subtraction of Li-produced components.
$^3He_{sp\ (z=0)}$ after correction for sampling depth (if necessary); ^4He_m = measured during heating; Eq. Rad. = mean equivalent spherical radius calculated following Farley et al. (1996).

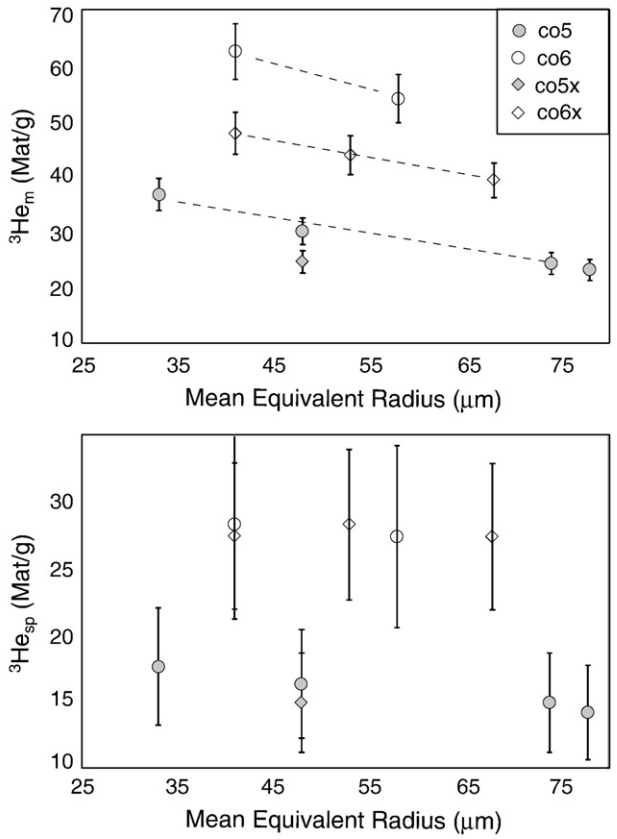

Fig. 2. Relationship between grain-size and measured ^{3}He (^3He_m) in zircon (upper panel), and the same relationship after correction for Li-produced ^{3}He ($^3He_{sp}$, lower panel). The grain-size relationship is due to the implantation of Li-produced and spallation produced ^{3}He from neighboring mineral phases.

each phase range between 0.48 and 0.59, similar to the value of 0.53 obtained for ^{10}Be in quartz. If a large non-cosmogenic component were present in *subequal concentrations* in the two different samples, it would skew the observed $^3He_{co\text{-}5/5x}/^3He_{co\text{-}6/6x}$ ratio. Likewise, the concentrations of ^{3}He in different phases within each sample are roughly equal, implying that the different phases do not contain a large non-cosmogenic component of *variable concentration*.

Nevertheless the Li contents in each of the mineral phases and in their host phases are high enough that a correction for Li-produced ^{3}He is required before estimating a production rate. In addition, we observe a strong correlation between measured ^{3}He and grain size in zircon (Fig. 2), implying that there is a significant implanted ^{3}He component, either Li or spallation-produced, that needs to be accounted for.

The amount of spallation-produced ^{3}He in each sample can be expressed as:

$$^3He_{sp} = {}^3He_m - {}^3He_{in} - {}^3He_{nuc} - {}^3He_{cn} - {}^3He_{mu} \quad (1)$$

where $^3He_{sp}$ is the ^{3}He produced via cosmic ray spallation, ^3He_m is the total ^{3}He measured in the sample, $^3He_{in}$ is inherited from inclusions or prior exposure, $^3He_{nuc}$ is the nucleogenic component produced by capture of neutrons produced from (α,n) reactions on light elements, $^3He_{cn}$ is the ^{3}He produced by capture of slow neutrons derived from interactions with "secondary" cosmogenic neutrons, and $^3He_{mu}$ is produced directly from stopping of slow muons and from capture of slow neutrons derived from muon interactions.

5.2. The magmatic He component

Assuming our samples did not experience prior exposure, the inherited ^{3}He component ($^3He_{in}$) is only magmatic. For uncrushed mineral phases (other than apatite and zircon), the magmatic component is taken as the concentration of ^{3}He released during crushing of other aliquots of the same mineral separate, and is subtracted from the measured ^{3}He (^3He_m) in uncrushed samples to give the crush-corrected ($^3He_{cc}$) value (Table 3). For samples that were crushed prior to fusion, it is assumed that the entire magmatic component was released during crushing, and no correction is made. This differs from the typical approach used to calculate the magmatic component, which is to calculate $^3He_{in} = {}^4He_{fusion} * (^3He/^4He)_{crush}$ implicitly assuming that all ^{4}He in the fused sample is magmatic (Kurz, 1986; Blard and Farley, 2008; Blard and Pik, 2008). This approach is not appropriate here because the measured ^{4}He concentrations in our pyroxene and olivine samples are high and variable, leading to erroneous corrections. Variability in ^{4}He concentration may be attributed to the presence of mineral inclusions or to implanted ^{4}He from high U and/or Th phases that were intergrown with pyroxene and olivine. The approach used in this study is a reasonable alternative based on the fact that replicate crushings of pyroxenes from sample co-5x and co-6x released comparable amounts of ^{3}He, and because correction of uncrushed samples by this approach brings the resultant ^{3}He concentrations into good agreement with crushed samples (Table 3). For apatite and zircon, the $^3He_{in}$ component is assumed to be negligible because the grain size is too small for significant fluid inclusion retention.

5.3. Quantifying Li-produced ^{3}He components

To calculate each Li-produced component, we follow the procedure described in Amidon et al. (2008a), which is described and applied in Appendix A of this paper. These calculations reveal that the total Li-produced ^{3}He ($^3He_{cn}$, $^3He_{mu}$, and $^3He_{nuc}$) for pyroxene and olivine varies, but is ~4 and ~6.5 Mat/g for co-5/5x and co-6/6x respectively (Table 3), or about 12–20% of the matrix-sited ^{3}He ($^3He_{cc}$). For garnet, this number is ~7.2 Mat/g, or ~27% of the measured ^{3}He. The difference between samples co-5/5x and co-6/6x is due to the different $^3He_{cn}$ components which result from using the different steady-state erosion rates inferred from the ^{10}Be results. Because the Coso samples have a young eruptive age and a long exposure duration, the $^3He_{nuc}$ component is about 1/3 the size of the $^3He_{cn}$ component. Neutrons produced from fast muon stopping and direct production of ^{3}He from fast muons are found to be negligible, whereas neutrons derived from stopping of slow muons account for ~20% of the total Li-derived ^{3}He.

In zircon the total Li-produced ^{3}He concentrations are grain size dependent, and reach maxima of ~19 and ~35 Mat/g for samples co-5/5x and co-6/6x respectively (Table 4). For apatite, values of 6.4 and 10.5 Mat/g are estimated for co-5x and co-6x respectively. Because the magnitude of the Li-produced ^{3}He component is grain size dependent, subtraction of this component reduces the slope of the correlation between grain size and ^{3}He for zircon (Fig. 2). This grain size effect is not important for larger grain sizes (i.e., olivine, pyroxene and garnet), and is not observable in apatite because only one grain size fraction was analyzed.

Uncertainties on the Li-produced ^{3}He estimates were calculated using a Monte Carlo simulation in which 11 variables were allowed to vary with a 1σ standard deviation of 15% over 1000 trials. These variables include internal Li content of the mineral, average Li content of adjacent minerals, bulk rock concentrations of the trace elements that strongly modulate neutron production or absorption (H, Li, B, Gd, Sm, U and Th), grain radius, and erosion rate. Although the major elements Si, K, Na and Al account for ~50% of neutron absorption, their published concentrations in the Devil's Kitchen rhyolite are unlikely to be wrong by more than a few relative percent and they are not included in the error analysis. For the coarser mineral phases (pyroxene, olivine, and garnet), a 15% standard deviation for each of the 11 input variables translates through the Monte Carlo model to a ~21% standard deviation in total Li-produced ^{3}He. Zircon and apatite

Table 5
Neon analyses in quartz and pyroxene.

Sample	Mass (g)	$^{20}Ne_m$ (Mat/g)	1σSD (Mat/g)	$^{21}Ne_m$ (Mat/g)	1σSD (Mat/g)	$^{22}Ne_m$ (Mat/g)	1σSD (Mat/g)	$\frac{^{21}Ne}{^{20}Ne}$	$\frac{^{22}Ne}{^{20}Ne}$	$^{21}Ne_{air}$ (Mat/g)	$^{21}Ne_{nuc}$ (Mat/g)	$^{21}Ne_c$ (Mat/g)	$^{21}Ne_{c\,(z=0)}$ (Mat/g)	1σSE (Mat/g)	^{10}Be (Mat/g)	1σSD (Mat/g)	$\frac{^{21}Ne_c}{^{10}Be}$	^{21}NE PR (at $g^{-1}a^1$)	1σ SE (at $g^{-1}a^1$)
co5-Q1	0.5124	6371	85.5	21.4	1.0	649	13.0	0.0034	0.1019	18.85	0.00	2.52	2.52						
co5-Q2	0.4802	6271	87.0	20.7	0.9	642	12.8	0.0033	0.1023	18.56	0.00	2.19	2.19						
co5-Q3	0.3306	6339	84.0	21.0	1.0	652	13.0	0.0033	0.1028	18.76	0.00	2.29	2.29						
co5-Q4	0.2565	1292	25.8	5.9	0.4	134	5.4	0.0046	0.1040	3.82	0.00	2.09	2.09						
Mean												**2.27**	**2.27**	**0.11**	**0.637**	**0.015**	**3.57**	**17.4**	**1.2**
co6-Q1	0.5053	3864	75.3	16.3	0.6	402	8.0	0.0042	0.1040	11.43	0.00	4.83	4.83						
co6-Q2	0.3278	6526	117.5	23.9	1.1	674	13.5	0.0037	0.1033	19.31	0.00	4.63	4.63						
co6-Q3	0.2563	1265	38.0	7.9	0.3	133	4.7	0.0062	0.1053	3.74	0.00	4.15	4.15						
co6-Q4	0.2559	5850	114.1	21.4	0.9	602	12.0	0.0037	0.1029	17.31	0.00	4.14	4.14						
co6-Q5	0.2542	1728	51.8	9.6	0.5	179	6.3	0.0055	0.1034	5.11	0.00	4.46	4.46						
Mean												**4.44**	**4.44**	**0.15**	**1.201**	**0.019**	**3.70**	**18.0**	**1.1**
														Weighted mean quartz			***3.63***	***17.7***	***0.8***
Co5x-P1	0.4053	4733	92.3	18.0	0.8	484	9.7	0.0038	0.1023	14.01	0.07	3.88	4.36	0.87	0.637	0.015	6.84	33.3	7.0
Co6x-P1	0.2433	2158	48.6	14.1	0.8	227	4.5	0.0066	0.1053	6.39	0.14	7.61	8.18						
Co6x-P2	0.2443	7881	130.0	30.6	1.3	814	16.3	0.0039	0.1033	23.32	0.14	7.12	7.65						
Co6x-P3	0.1070	3282	73.8	17.0	0.9	341	6.8	0.0052	0.1039	9.71	0.14	7.15	7.69						
Mean												**7.29**	**8.42**	**0.21**	**1.201**	**0.019**	**7.01**	**34.2**	**1.7**
														Weighted mean pyroxene			***7.08***	***34.1***	***1.6***
Co5-Qincl.	0.0071	286757	4302	736.2	35.2	26434	528.6	0.0026	0.0922										
Co6-Qincl.	0.0508	44538	667.5	133.4	6.4	4445	88.8	0.003	0.0998										
co5x-Plaser	0.1776	1285	38	5.2	0.5	114	3.85	0.0041	0.0885										
co6x-Plaser	0.1025	3582	81	27.9	1.2	254	7.5	0.0078	0.0709										

$^{21}Ne_{air}$ = concentration of ^{21}Ne derived from air contamination of sample; $^{21}Ne_{nuc}$ = concentration of ^{21}Ne calculated from reactions $^{18}O(\alpha,n)^{21}Ne$ and $^{24}Mg(n,\alpha)^{21}Ne$.
$^{21}Ne_c$ = concentration of cosmogenic ^{21}Ne remaining after subtraction of $^{21}Ne_{air}$ and $^{21}Ne_{nuc}$ components from measured component ($^{21}Ne_m$).
"Qincl" denotes inclusion-bearing quartz samples; "Plaser" denotes pyroxene samples fused with a Nd-YAG laser.

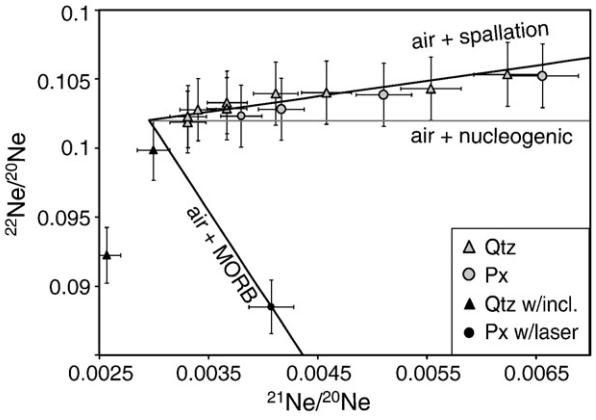

Fig. 3. Neon three-isotope diagram showing that most Coso samples plot along an air-spallation mixing line. Grey symbols represent data used to calculate the ^{21}Ne production rate. Black symbols show analyses of inclusion bearing quartz (triangles) and pyroxene fused with laser (circles), which contain significant non-cosmogenic neon components and thus plot away from the air-spallation mixing line for quartz, with slope of 1.12 (Niedermann, 2002).

are more sensitive to uncertainties in grain size and host Li content, and thus have ~25% standard deviations on the total Li-produced ^{3}He.

An additional source of uncertainty arises from our interpretation of the ^{10}Be concentrations as steady-state erosion rates. This interpretation affects calculated spallation ^{3}He production rates in two ways: 1) the size of the $^{3}He_{cn}$ component, and 2) the possibility of ^{10}Be decay over time. To explore the sensitivity of our ^{3}He production rates to our interpreted erosional history, we consider two end-member alternatives. In the "uneroded surface" case, the surfaces were instantaneously exhumed from >3 m depth at the time of their apparent ^{10}Be exposure age and remained uneroded. In this case, the $^{3}He_{cn}$ component is 25–40% higher than in the steady-state erosion case, and ^{10}Be decay remains insignificant. In the "uneroded and buried surface" case, surfaces were exposed immediately after eruption for the duration of their ^{10}Be exposure ages and then buried abruptly until being instantly exhumed in the very recent past. In this case, the $^{3}He_{cn}$ components would again be 25–40% higher, and ~25% of the ^{10}Be would have decayed during burial. When production rates are calculated assuming these alternative exhumation models, both models show a negative relationship between production rate and apparent Li (Fig. 4). This relationship suggests that these non steady-state models result in overcorrection for the Li-produced component. Additionally, when plotted on a diagram of ^{10}Be/^{21}Ne vs ^{10}Be concentration, both samples fall within error of the steady-state erosion regime (Lal, 1991).

5.4. Cosmogenic ^{3}He production rates

Subtracting the Li-produced ^{3}He improves agreement in production rate among all phases, demonstrating that the calculations are

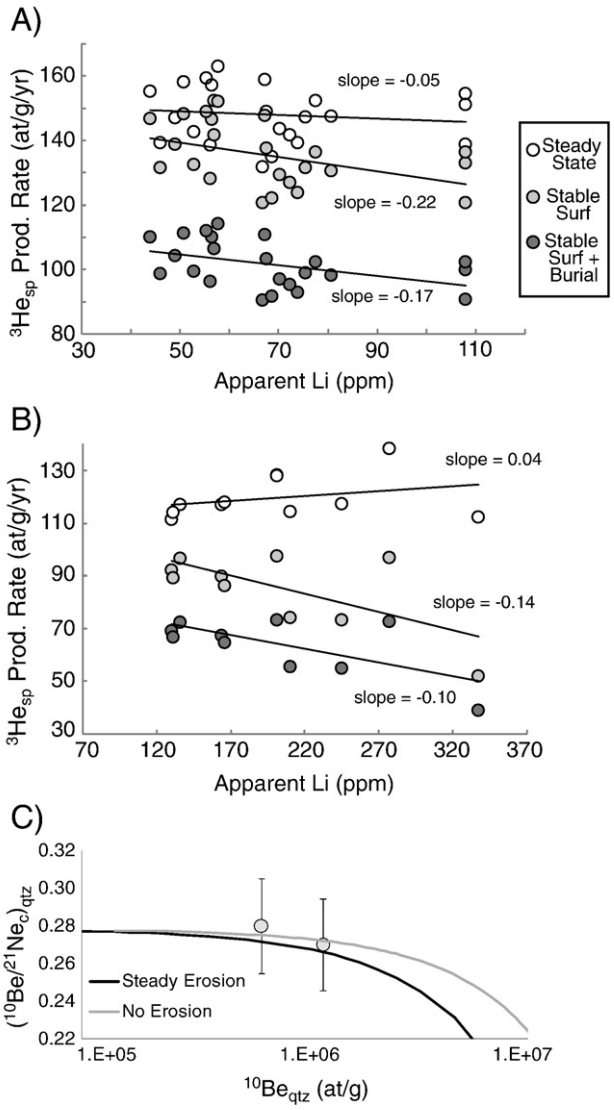

Fig. 4. Spallation ^{3}He production rate versus apparent Li for all pyroxene, olivine and garnet analyses (panel A), and for all zircon analyses (panel B). Open symbols were corrected for Li-produced ^{3}He components assuming a steady-state erosional history as described in the text, and reported in the data tables. Grey circles are calculated assuming an alternative exhumational history in which the surface was exposed at the ^{10}Be exposure age, and remained uneroded until today. Black symbols are calculated assuming a second alternative scenario in which the surface was exposed immediately after eruption for the duration of the ^{10}Be exposure age, then buried for ~560 ka, and abruptly re-exhumed in very recent times causing ~25% of the^{10}Be to decay. The negative slopes of the two alternative exhumation histories show that these interpretations would lead to over-correction for the Li-produced ^{3}He component. Panel C shows that our two samples fall within 2σ error of the steady-state erosion island defined by Lal (1991), using SLHL production rates of 4.87 and 17.7 at g^{-1} a^{-1} for ^{10}Be and ^{21}Ne respectively, and a scaling factor of 2.75.

Table 6
Li concentrations (ppm).

	co5	co6	co5x	co6x	co5i
Pyroxene	53	28	17	10	–
Olivine	26	32	23	25	–
Magnetite	19	–	22	–	–
Hornblende	435	327	–	–	–
Quartz	93	99	–	–	32
Feldspar	141	139	27	19	184
Biotite	5070	8576	2100	2490	–
Zircon	10.2	4.8	1.4	1.5	–
Apatite	–	–	15.0	16.5	–
Garnet	–	–	–	–	108
Matrix	153	159	423	513	–

co5i denotes the garnet-plag-qtz xenolith.

reasonable (Tables 3 and 4). Pyroxene, olivine and garnet give mean $^{3}He_{sp}$ concentrations of ~18.4 and ~35.5 Mat/g for samples co-5/5x and co-6/6x respectively (Fig. 1). By taking the $^{3}He_{sp}/^{10}$Be ratio and multiplying by an average ^{10}Be production rate of 4.87 at g^{-1} a^{-1} (Balco et al., 2008), grand mean production rates of 145 ± 11, 141 ± 16, and 144 ± 30 at g^{-1} a^{-1} (2σ) are calculated for pyroxene, olivine, and garnet respectively. Zircon gives mean $^{3}He_{sp}$ concentrations of 15.4 and 27.7 Mat/g for co-5/5x and co-6/6x respectively, averaged over equivalent radii from 33–78 μm. Apatite gives 19.5 and 36.6 Mat/g respectively for equivalent radii of ~100 μm (Fig. 2). Repeating the above calculation, the mean apparent production rates for zircon and apatite are 114 ± 8 and 149 ± 28 at g^{-1} a^{-1} (2σ).

Errors on production rates are derived from the quadratic propagation of errors on $^{3}He_{sp}$, the ^{10}Be measurement, and the ^{10}Be production rate. The standard errors on $^{3}He_{sp}$ for pyroxene, olivine, garnet and apatite were calculated by taking the standard error on replicate measurements of $^{3}He_{cc}$ for a given phase and propagating it in quadrature with the constant Monte-Carlo error on the Li–^{3}He component for that phase. The 1σ standard error on the ^{10}Be production rate is taken from Balco et al. (2008) as 4.87 ± 0.26. Because estimates of Li-produced ^{3}He are grain size dependent for zircon, we calculate errors on $^{3}He_{sp}$ for each analysis individually, take the standard error of all analyses for a given sample, and then propagate this with the ^{10}Be measurement error and the ^{10}Be production rate error. The weighted mean of all samples for a given mineral phase is then computed as well as the weighted mean error, and reported above. This analysis ignores systematic errors associated with instrument calibration, as they are thought to be <1% (Min et al., 2003).

5.5. Cosmogenic ^{21}Ne production rates

The amount of cosmogenic ^{21}Ne ($^{21}Ne_c$) is calculated by:

$$^{21}Ne_c = {}^{21}Ne_m - {}^{21}Ne_{air} - {}^{21}Ne_{nuc} \quad (2)$$

where $^{21}Ne_m$ is the measured ^{21}Ne in the sample, $^{21}Ne_{air}$ is the ^{21}Ne derived from trapped air components, and $^{21}Ne_{nuc}$ is the ^{21}Ne produced by nucleogenic sources, primarily the reactions $^{18}O(\alpha,n)^{21}Ne$ and $^{24}Mg(n,\alpha)^{21}Ne$.

Assuming that all ^{20}Ne is derived from air allows the $^{21}Ne_{air}$ component to be calculated by:

$$^{21}Ne_{air} = {}^{20}Ne_m \times \left(\frac{^{21}Ne}{^{20}Ne}\right)_{air} \quad (3)$$

where $(^{21}Ne/^{20}Ne)_{air}$ is the known ratio of 0.002959 in air (Niedermann, 2002).

Because quartz has very little U and Th (the primary sources of α particles), $^{21}Ne_{nuc}$ is assumed to be zero. Neon produced by implanted α particles cannot be ruled out although a >300 μm grain diameter and HF leaching should minimize this component (Kohl and Nishiizumi, 1992). However, because pyroxenes can contain moderate amounts of U and Th (Blard and Pik, 2008) and because they are retentive to helium, the amount of radiogenic ^{4}He can be used to make a rough estimate of $^{21}Ne_{nuc}$ based on the relationship:

$$^{21}Ne_{nuc} / {}^{4}He = 5.2 \times 10^{-8} \times F_0 \quad (4)$$

where F_0 is the mass fraction of oxygen in the mineral (Eikenberg et al., 1993). The mass fraction of oxygen in the pyroxenes is ~0.43, and average ^{4}He concentrations are 1.7×10^{12} and 3.8×10^{12} at/g, yielding a $^{21}Ne_{nuc}$ component of 0.038 and 0.085 Mat/g for co-5x and co-6x respectively, or ~1.2% in both cases. We also consider ^{21}Ne production via the reaction $^{24}Mg(n,\alpha)^{21}Ne$, which has a cutoff energy of ~3 MeV, and a resonance integral of ~0.0054 barn (Nakagawa et al., 2002). An approximate calculation of ^{21}Ne derived from neutron capture by ^{24}Mg can be made by multiplying the radiogenic and cosmogenically derived neutron fluxes (supplementary Table A3) by the resonance integral and by the atomic density of ^{24}Mg in pyroxene. This calculation yields ~0.006 Mat/g of production from radiogenic neutrons, and ~0.024 and 0.053 Mat/g of production from cosmogenically derived thermal neutrons in samples co-5 and co-6 respectively.

After subtraction of the small nucleogenic component, production rates of ^{21}Ne are calculated by multiplying the $^{21}Ne_c/^{10}Be$ ratio by the stated ^{10}Be production rate. Averages of all analyses are 17.7 ± 1.6 and 34.1 ± 3.2 at g^{-1} a^{-1} (2σ) in quartz and pyroxene respectively (Table 5). The higher value in pyroxene arises from the presence of Mg and Al, which produce more ^{21}Ne than does Si (Leya et al., 1998). Errors for a given sample are calculated by determining the standard error on replicate estimates of $^{21}Ne_c$ and propagating this in quadrature with errors on the measured ^{10}Be and the ^{10}Be production rate. The weighted mean of all samples for a given mineral phase is then computed as well as the weighted mean error.

6. Discussion

6.1. ^{3}He production rates

Our SLHL production rates of 145 ± 11 and 141 ± 16 at g^{-1} a^{-1} (2σ) in pyroxene and olivine are higher than the highest value of 122 ± 14 at g^{-1} a^{-1} (1σ) reported by Balco et al. (2008) scaled following Lifton et al. (2005). However, our results are similar to those of Ackert et al. (2003), which were attributed to anomalously low air pressure over the study area. Our values are slightly higher than those of Blard et al. (2006), and are somewhat lower than the average of 159 at g^{-1} a^{-1} for olivine and pyroxene calculated from element specific production rates (Kober et al., 2005). Our production rate of 144 ± 30 at g^{-1} a^{-1} in garnet is lower than the value of 153 at g^{-1} a^{-1} reported by Amidon et al. (2008a) and 154 at g^{-1} a^{-1} which they recalculate from the data of Gayer et al. (2004). This lower value is consistent (although not perfectly) with the apparent overproduction observed at high-elevation in Nepal by both of these studies, and matches the production rate calculated from element-specific production rates of 145 at g^{-1} a^{-1} (Kober et al., 2005).

Our results for pyroxene and olivine thus contribute to the surprisingly wide range of estimated ^{3}He production rates in these phases. One possible explanation for our higher values relative to those summarized in Balco et al. (2008) is that we compare ^{3}He directly to ^{10}Be, rather than to a surface exposure age inferred from the crystallization age of a lava flow. We thus avoid the assumption that the sampled flow is uneroded and has never experienced burial, both of which would lower the apparent ^{3}He production rate in a calibration study. We also avoid the assumption that all ^{4}He released during fusion of a crushed pyroxene or olivine sample is derived from a mantle component. Studies which follow this procedure, without measuring the U and Th contents of the pyroxene or olivine, may be subject to overcorrection for mantle ^{3}He (Blard and Farley, 2008; Blard and Pik, 2008). Because these corrections can be as large as 90%, this could lead to a significant underestimate of the amount of cosmogenic ^{3}He in a sample.

For zircon and apatite, we estimate mean apparent production rates of 114 ± 8 and 149 ± 28 at g^{-1} a^{-1}, for equivalent radiii of 40–80 μm in zircon, and 100 μm in apatite. Since the first estimates of production rates in these minerals were published by Farley et al. (2006), a ^{10}Be analysis has been obtained on quartz from their sample C3_C4 (Table 1). Calculating $^{3}He/^{10}Be$ ratios for sample C3_C4, and multiplying by a ^{10}Be production rate of 4.87 at g^{-1} a^{-1}, gives apparent production rates of 111 ± 22, 141 ± 28 and 123 ± 15 at g^{-1} a^{-1} (2σ) for zircon, apatite, and titanite. A subsequent study by Amidon et al. (2008a) proposes an elevation dependent production rate in Nepal, and the lowest elevation sample in their dataset, sample CRN-259 (3215 m), gives apparent production rates of 134 ± 26 and 166 ± 32 at g^{-1} a^{-1} (2σ) for zircon and apatite respectively. Thus it appears that results from the current study are in good agreement with results from Bolivia, but somewhat lower than results from Nepal (Farley et al., 2006; Amidon et al., 2008a).

We use the term apparent production rates for zircon and apatite because we have not accounted for redistribution of spalled ^{3}H and ^{3}He nuclei among adjacent grains. Because adjacent silicate minerals have higher spallation production rates than in zircon and apatite, a negative correlation between grain-size and $^{3}He_{sp}$ is expected in these phases (Farley et al., 2006). Zircons from sample co-5 show a linear correlation ($r^2 = 0.98$) between mean equivalent radius (MER) and apparent

production rate (APR) described by the linear fit APR = −0.55*MER + 156. The apparent production rate in grains with MER of 78 μm is about 20% lower than in grains with MER of 33 μm. A grain size experiment on zircons from Himalayan gneisses also resulted in ~20% lower production rates between mean widths of 38 and 100 μm, whereas results from zircons in a Bolivian ignimbrite showed ~10% decrease in production rate between widths of 50 and 100 μm (Farley et al., 2006; Amidon et al., 2008a). Future datasets may allow calculation of the spalled ^{3}He and ^{3}H stopping ranges, and thus of the in-situ ^{3}He production rate in zircon and apatite. However, the present data suggest that ^{3}He dating in apatite and zircon can be undertaken using apparent production rates in coarser grain size fractions.

6.2. ^{21}Ne production rates in quartz and pyroxene

The ^{21}Ne production rate of 17.7 ± 1.6 at g^{-1} a^{-1} (2σ) we obtain for quartz is within error of all previous calibration studies. This value is 7% less than the value of 19.0 ± 3.7 (2σ) reported by Niedermann (2000) and similar to a value of 17.7 ± 2.6 at g^{-1} a^{-1} that they rescaled from a study of quartz targets exposed for three years at an elevation of 4250 m on Mt. Evans, CO (Graf et al., 1996). Likewise, a recent study that exposed quartz targets over a range of elevation in the Alps for one year found ^{21}Ne production rates of 16.9 ± 1.9 at g^{-1} a^{-1} (2σ) (Vermeesch et al., 2008). Our $^3He_{px}/^{21}Ne_{qtz}$ ratio (~8.2) and our $^3He_{px}/^{21}Ne_{qtz}$ ratio (~8.0) are identical to the values reported from a basaltic andesite in Argentina (Niedermann et al., 2007). The ^{21}Ne production rate of 34.1 ± 3.2 at g^{-1} a^{-1} (2σ) we calculate in pyroxene gives a $^{21}Ne_c/^3He_{sp}$ ratio of ~0.235, which is similar to the ratio of 0.236 measured in Antarctic pyroxenes (Bruno et al., 1997; Schafer et al., 1999). This ratio is also similar to ratios of 0.19–0.20 reported from pyroxenes in a Pleistocene lava flow in the western United States (Fenton et al., 2007).

One reason ^{21}Ne production rates may vary between studies is if the neon inventory is not a simple mixture of cosmogenic, nucleogenic and air-derived neon. When our data are plotted on a three-isotope diagram (Fig. 3), most samples plot near the air–cosmogenic mixing line, suggesting they contain only these three components. However, the hand-picked inclusion-bearing quartz samples, and the two pyroxene samples fused with the laser plot closer to the air–MORB mixing line suggesting that they may also contain a mantle-derived neon component. The fact that pyroxene samples fused with the laser plot near the MORB mixing line, but pyroxene samples heated with the furnace plot near the cosmogenic mixing line suggests that the pyroxenes contain a mantle component which is only released by complete fusion of the crystal (Staudacher and Allegre, 1993). A similar release pattern for mantle-derived neon has been observed in some previous studies (Niedermann, 2002).

6.3. An alternate method of calculating Li-produced ^{3}He

The labor-intensive approach to calculating the Li-produced ^{3}He components used in this study (see Appendix A) involves point counting of adjacent minerals, Li measurement in all mineral phases, and documentation of average grain size for each sample. A simpler alternative is to measure $^3He_{nuc}$ in a shielded sample. At face value, this is of limited use because the shielded minerals do not contain the potentially larger $^3He_{cn}$ component produced in the near-surface. However, if the petrology and grain size of the shielded and exposed samples are identical, we can use the shielded ^{3}He concentration, the (U–Th)/He closure age, the bulk rock composition, and a neutron production–diffusion model to solve for the grain-size specific apparent Li. Significant time and effort are saved because it is not necessary to measure Li in any mineral phases or to document the distribution of adjacent minerals.

For uneroded surfaces or for surfaces experiencing steady-state erosion, the apparent Li of a mineral determined from the shielded sample can be used to calculate the $^3He_{cn}$ component acquired in the near-surface. Assuming the exposure age or erosion rate of a surface is unknown, and neglecting the muogenic component, the $^3He_{cn}$ concentration is given by:

$$^3He_{cn} = \left(^3He_m - {}^3He_{nuc}\right) * \frac{^3He_{cn}}{\left(^3He_{cn} + {}^3He_{sp}\right)} \quad (5)$$

where ^3He_m is the measured ^{3}He concentration in the surface sample, and $^3He_{sp}$ is the unknown concentration of spallation produced ^{3}He. For an uneroded surface, the ratio in the second term in Eq. (5) is independent of exposure age and is given by:

$$\frac{^3He_{cn}}{\left(^3He_{cn} + {}^3He_{sp}\right)} = \frac{P_{cn}(0)}{\left(P_{cn}(0) + P_{sp}(0)\right)} \quad (6)$$

Where the spallation production rate $P_{sp}(0)$ is assumed to be known, and the CN production rate $P_{cn}(0)$ can be calculated using the apparent Li and a neutron production–diffusion model (see Appendix A). In cases of steady erosion over a time-scale sufficient to have exhumed more than ~800 g/cm^2, the second term in Eq. (5) is also independent of erosion rate and is given by:

$$\frac{^3He_{cn}}{\left(^3He_{cn} + {}^3He_{sp}\right)} = \frac{\int P_{cn}(z)dz}{\left(\int P_{cn}(z)dz + \int P_{sp}(z)dz\right)} \quad (7)$$

where the shape of the $P_{cn}(z)$ profile can also be computed using a neutron-production diffusion model and the apparent Li of the mineral.

7. Conclusions

This study calibrates the production rates of cosmogenic ^{3}He and ^{21}Ne in common minerals against ^{10}Be in quartz from a rhyolite dome in the Coso volcanic field. We show that Li-produced ^{3}He components can be large, but when subtracted from measured ^{3}He give results comparable to previous studies. Although our approach is vulnerable to systematic errors associated with modeling neutron production and diffusion, our results appear robust based on comparisons across different samples, mineral phases, and isotope systems. At face value our new production rates of ~143 at g^{-1} a^{-1} for olivine and pyroxene lie at the high end of previous estimates. This indicates that the complexities of spallogenic ^{3}He (and ^{3}H) production remain an open research question.

Zircon and apatite show promise as target phases for ^{3}He dating due to their ubiquity, relatively low Li contents, and lack of magmatic ^{3}He components. The Li-produced components in zircon and apatite can be minimized by working with lithologies that have large grain sizes, young U/Th–He closure ages, and low U, Th and Li contents. We also estimate production rates of ^{21}Ne to be 17.7 ± 1.6 and 34.1 ± 3.2 at g^{-1} a^{-1} for quartz and pyroxene respectively. These results agree well with previous production rates, and demonstrate that cosmogenic ^{21}Ne dating can be accomplished in rocks high in U and Th, it least if they are relatively young.

Acknowledgements

Thanks to Don Burnett, P.H. Blard, and Frank Monastero. Thanks to Samuel Niedermann and an anonymous reviewer for greatly improving this manuscript. This work was supported by National Science Foundation Grant 0511053.

Appendix A. Supplementary data

Supplementary data associated with this article can be found, in the online version, at doi:10.1016/j.epsl.2009.01.031.

References

Ackert, R.P., Singer, B.S., Guillou, H., Kaplan, M.R., Kurz, M.D., 2003. Long-term cosmogenic ^{3}He production rates from ^{40}Ar/^{39}Ar and K–Ar dated Patagonian lava flows at 47°S. Earth Planet. Sci. Lett. 210, 119–136.

Amidon, W., Farley, K.A., Burbank, D.W., Pratt-Sitaula, B., 2008a. Anomalous cosmogenic ^{3}He production and elevation scaling in the high Himalaya. Earth Planet. Sci. Lett. 265, 287–301.

Amidon, W.H., Farley, K.A., Hynek, S.A., 2008b. A field test of cosmogenic ^{3}He dating in calcite. Abstr. Programs — Geol. Soc. Am. 40.

Andrews, J.N., Kay, R.L.F., 1982. Natural production of tritium in permeable rocks. Nature 298, 361–363.

Bacon, C.R., Metz, J., 1984. Magmatic inclusions in rhyolites, contaminated basalts, and compositional zonation beneath the Coso volcanic field, California. Contrib. Mineral. Petrol. 85, 346–365.

Bacon, C.R., Duffield, W.A., Nakamura, K., 1980. Distribution of Quaternary rhyolite domes of the Coso Range, California — implications for extent of the geothermal anomaly. J. Geophys. Res. 85, 2425–2433.

Bacon, C.R., Macdonald, R., Smith, R.L., Baedecker, P.A., 1981. Pleistocene high-silica rhyolites of the Coso volcanic field, Inyo County, California. J. Geophys. Res. 86, 223–241.

Balco, G., Stone, J.O., Lifton, N.A., Dunai, T.J., 2008. A simple, internally consistent, and easily accessible means of calculating surface exposure ages or erosion rates from ^{10}Be and ^{26}Al measurements. Quat. Geochronol. 3, 174–195.

Bierman, P.R., 1994. Using in-situ produced cosmogenic isotopes to estimate rates of landscape evolution— a review from the geomorphic perspective. J. Geophys. Res.-Solid Earth 99, 13885–13896.

Blard, P.H., Farley, K.A., 2008. The influence of radiogenic ^{4}He on cosmogenic ^{3}He determinations in volcanic olivine and pyroxene. Earth Planet. Sci. Lett. 226, 20–29.

Blard, P.H., Pik, R., 2008. An alternative isochron method for measuring cosmogenic ^{3}He in lava flows. Chem. Geol. 251, 20–32.

Blard, P.H., Pik, R., Lave, J., Bourles, D., Burnard, P.G., Yokochi, R., Marty, B., Trusdell, F., 2006. Cosmogenic ^{3}He production rates revisited from evidence of grain size dependent release of matrix-sited helium. Earth Planet. Sci. Lett. 247, 222–234.

Bruno, L.A., Baur, H., Graf, T., Schluchter, C., Signer, P., Wieler, R., 1997. Dating of Sirius Group tillites in the Antarctic Dry Valleys with cosmogenic ^{3}He and ^{21}Ne. Earth Planet. Sci. Lett. 147, 37–54.

Bryce, J.G., Farley, K.A., 2002. ^{3}He exposure dating of magnetite. Geochim. Cosmochim. Acta 66, A108.

Cerling, T., Craig, H., 1994. Cosmogenic ^{3}He production rates from 39N to 46N latitude, western USA and France. Geochim. Cosmochim. Acta 58, 249–255.

Copeland, P., Watson, E.B., Urizar, S.C., Patterson, D., Lapen, T.J., 2007. Alpha thermochronology of carbonates. Geochim. Cosmochim. Acta 71, 4488–4511.

Dunai, T.J., Roselieb, K., 1996. Sorption and diffusion of helium in garnet: Implications for volatile tracing and dating. Earth Planet. Sci. Lett. 139, 411–421.

Dunai, T., Wijbrans, J., 2000. Long-term cosmogenic ^{3}He production rates (152 ka–1.35 Ma) from ^{40}Ar/^{39}Ar dated basalt flows at 29°N latitude. Earth Planet. Sci. Lett. 176, 147–156.

Dunai, T., Stuart, F.M., Pik, R., Burnard, P.G., Gayer, E., 2007. Production of ^{3}He in crustal rocks by cosmogenic thermal neutrons. Earth Planet. Sci. Lett. 258, 228–236.

Eikenberg, J., Signer, P., Wieler, R., 1993. U–Xe, U–Kr and U–Pb systematics for dating U minerals and investigations of the production of nucleogenic Ne and Ar. Geochim. Cosmochim. Acta 57, 1053–1069.

Farley, K.A., 2002. (U–Th)/He dating: Techniques, calibrations, and applications. Noble Gases in Geochemistry and Cosmochemistry. Mineralogical Soc America, Washington, pp. 819–844.

Farley, K.A., Liabarkin, J., Mukhopadhyay, S., Amidon, W., 2006. Cosmogenic and nucleogenic ^{3}He in apatite, titanite, and zircon. Earth Planet. Sci. Lett. 248, 436–446.

Farley, K.A., Wolf, R.A., Silver, L.T., 1996. The effects of long alpha-stopping distances on (U–Th)/He ages. Geochim. Cosmochim. Acta 60, 4223–4229.

Fenton, C.R., Niedermann, S., Goethals, M., Schneider, B., 2007. Cosmogenic Ne-21/He-3 in olivines and pyroxenes from a Pleistocene basalt flow, Western Grand Canyon National Park, Arizona, USA. Geochim. Cosmochim. Acta 71, A272.

Gayer, E., Lavé, J., Pik, R., France-Lanord, C., 2006. Monsoonal forcing of Holocene glacier fluctuations in Ganesh Himal (Central Nepal) constrained by cosmogenic ^{3}He exposure ages of garnets. Earth Planet. Sci. Lett. 252, 275–288.

Gayer, E., Pik, R., Lave, J., France-Lanord, C., Bourles, D., Marty, B., 2004. Cosmogenic ^{3}He in Himalayan garnets indicating an altitude dependence of the ^{3}He/^{10}Be production ratio. Earth Planet. Sci. Lett. 229, 91–101.

Gosse, J., Phillips, F., 2001. Terrestrial in situ cosmogenic nuclides: theory and application. Quat. Sci. Rev. 20, 1475–1560.

Graf, T., Marti, K., Wiens, R.C., 1996. The ^{21}Ne production rate in a Si target at mountain latitudes. Radiocarbon 38, 155–156.

Heisinger, B., Lal, D., Jull, A.J.T., Kubik, P.W., Ivy-Ochs, S., Knie, K., Nolte, E., 2002a. Production of selected cosmogenic radionuclides by muons: 2. Capture of negative muons. Earth Planet. Sci. Lett. 200, 357–369.

Heisinger, B., Lal, D., Jull, A.J.T., Kubik, P.W., Ivy-Ochs, S., Neumaier, S., Knie, K., Lazarev, V., Nolte, E., 2002b. Production of selected cosmogenic radionuclides by muons: 1. fast muons. Earth Planet. Sci. Lett. 200, 345–355.

Kober, F., Ivy-Ochs, S., Leya, I., Baur, H., Magna, T., Wieler, R., Kubik, P.W., 2005. In situ cosmogenic ^{10}Be and ^{21}Ne in sanidine and in situ cosmogenic ^{3}He in Fe–Ti-oxide minerals. Earth Planet. Sci. Lett. 236, 404–418.

Kohl, C.P., Nishiizumi, K., 1992. Chemical isolation of quartz for measurement of in situ-produced cosmogenic nuclides. Geochim. Cosmochim. Acta 56, 3583–3587.

Kurz, M.D., 1986. In-situ production of terrestrial cosmogenic helium and some applications to geochronology. Geochim. Cosmochim. Acta 50, 2855–2862.

Kurz, M.D., Colodner, D., Trull, T.W., Moore, R.B., Obrien, K., 1990. Cosmic-ray exposure dating with in-situ produced cosmogenic ^{3}He: results from young Hawaiian lava flows. Earth Planet. Sci. Lett. 97, 177–189.

Lal, D., 1991. Cosmic ray labeling of erosion surfaces: in situ production rates and erosion models. Earth Planet. Sci. Lett. 104, 424–439.

Leya, I., Busemann, H., Baur, H., Wieler, R., Gloris, M., Neumann, S., Michel, R., Sudbrock, F., Herpers, U., 1998. Cross sections for the proton-induced production of He and Ne isotopes from magnesium, aluminum, and silicon. Nucl. Instrum. Methods Phys. Res., B Beam Interact. Mater. Atoms 145, 449–458.

Licciardi, J., Kurz, M.D., Clark, P., Brook, E., 1999. Calibration of cosmogenic ^{3}He production rates from Holocene lava flows in Oregon, USA, and effects of the Earth's magnetic field. Earth Planet. Sci. Lett. 172, 261–271.

Licciardi, J.M., Kurz, M.D., Curtice, J.M., 2006. Cosmogenic ^{3}He production rates from Holocene lava flows in Iceland. Earth Planet. Sci. Lett. 246, 251–264.

Lifton, N., Bieber, J., Clem, J., Duldig, M., Evenson, P., Humble, J., Pyle, R., 2005. Addressing solar modulation and long-term uncertainties in scaling secondary cosmic rays for in situ cosmogenic nuclide applications. Earth Planet. Sci. Lett. 239, 140–161.

Manley, C.R., Bacon, C.R., 2000. Rhyolite thermobarometry and the shallowing of the magma reservoir, Coso volcanic field, California. J. Petrol. 41, 149–174.

Miller, J.S., Wooden, J.L., 2004. Residence, resorption and recycling of zircons in Devils Kitchen rhyolite, Coso volcanic field, California. J. Petrol. 45, 2155–2170.

Min, K.W., Farley, K.A., Renne, P.R., Marti, K., 2003. Single grain (U–Th)/He ages from phosphates in Acapulco meteorite and implications for thermal history. Earth Planet. Sci. Lett. 209, 323–336.

Nakagawa, T., Kawasaki, H., Shibata, K., 2002. Curves and Tables of Neutron Cross Sections in JENDL-3.3. Japan Atomic Energy Research Institute, Tokyo.

Niedermann, S., 2000. The ^{21}Ne production rate in quartz revisited. Earth Planet. Sci. Lett. 183, 361–364.

Niedermann, S., 2002. Cosmic-ray-produced noble gases in terrestrial rocks: dating tools for surface processes. In: Porcelli, D., Ballentine, C.J., Wieler, R. (Eds.), Noble Gases in Geochemistry and Cosmochemistry. . Reviews in Mineralogy and Geochemistry, vol. 47. Mineralogical Society of America, Washington D.C., pp. 731–784.

Niedermann, S., Graf, T., Marti, K., 1993. Mass spectrometric identification of cosmic-ray produced ^{21}Ne in terrestrial quartz: the neon inventory of Sierra Nevada quartz separates. Earth Planet. Sci. Lett. 118, 65–73.

Niedermann, S., Pilz, P., Goethals, M., 2007. Assessing the relative production rates of cosmogenic He-3 and Ne-21 in olivine, pyroxene and quartz. Geochim. Cosmochim. Acta 71, A717.

Niishizumi, K., Imamura, M., Caffee, M., Southon, J.R., Finkel, R.C., McAninch, J., 2007. Absolute calibration of ^{10}Be AMS standards. Nucl. Instrum. Methods Phys. Res. B 258, 403–413.

Patterson, D.B., Farley, K.A., McInnes, B., 1997. Helium isotopic composition of the Tabar–Lihir–Tanga–Feni island arc, Papua New Guinea. Geochim. Cosmochim. Acta 61, 2485–2496.

Schafer, J., Ivy-Ochs, S., Wieler, R., Leya, I., Baur, H., Denton, G., Schluchter, C., 1999. Cosmogenic noble gas studies in the oldest landscape on earth: surface exposure ages of the Dry Valleys, Antarctica. Earth Planet. Sci. Lett. 167, 215–226.

Shuster, D.L., Farley, K.A., 2005. Diffusion kinetics of proton-induced Ne-21, He-3, and He-4 in quartz. Geochim. Cosmochim. Acta 69, 2349–2359.

Simon, J., Vazquez, J.A., Renne, P.R., Schmitt, A.K., Bacon, C.R., Reid, M.R., 2008. Accessory mineral U–Th–Pb ages and ^{40}Ar/^{39}Ar eruption chronology, and their bearing on rhyolitic magma evolution in the Pleistocene Coso volcanic field, California. Contrib. Mineral. Petrol. in review.

Staudacher, T., Allegre, C.J., 1993. The cosmic ray produced ^{3}He/^{21}Ne ratio in ultramafic rocks. Geophys. Res. Lett. 20, 1075–1078.

Vermeesch, P., Heber, V., Strasky, S., Kober, F., Schaefer, J., Baur, J., Schluchter, C., Wieler, R., 2008. Cosmogenic ^{3}He and ^{21}Ne measured in artificial quartz targets after one year of exposure in the Swiss Alps. Geophys. Res. Abstr. 10, EGU2008–A-08431.

Ziegler, J.F., 2003. Stopping and Range of Ions in Matter (SRIM), http://www.srim.org/.